Article

Cytochrome P450 3A4 Inhibition by Ketoconazole: Tackling the Problem of Ligand Cooperativity Using Molecular Dynamics Simulations and Free-Energy Calculations

Urban Bren[†,‡] and Chris Oostenbrink*[,†,§]

[†]Institute of Molecular Modeling and Simulation, University of Natural Resources and Life Sciences, Muthgasse 18, AT-1190 Vienna, Austria

[‡]Laboratory for Molecular Modeling, National Institute of Chemistry, Hajdrihova 19, SI-1001 Ljubljana, Slovenia

[§]Division of Computational and Molecular Toxicology, VU University, De Boelean 1083, 1081 HV Amsterdam, The Netherlands

S *Supporting Information*

ABSTRACT: Cytochrome P450 3A4 (CYP3A4) metabolizes more than 50% of clinically used drugs and is often involved in adverse drug–drug interactions. It displays atypical binding and kinetic behavior toward a number of ligands characterized by a sigmoidal shape of the corresponding titration curves, which is indicative of a positive homotropic cooperativity. This requires a participation of at least two ligand molecules, whereby the binding of the first ligand molecule increases the affinity of CYP3A4 for the binding of the second ligand molecule. In the current study, a combination of molecular dynamics simulations and free-energy calculations was applied to elucidate the physicochemical origin of the observed positive homotropic cooperativity in ketoconazole binding to CYP3A4. The binding of the first ketoconazole molecule was established to increase the affinity for the binding of the second ketoconazole molecule by 5 kJ mol^{-1}, which explains and quantifies the experimentally observed cooperative behavior of CYP3A4. Shape complementarity through nonpolar van der Waals interactions was identified as the main driving force of this binding, which seems to be in line with the promiscuous nature of CYP3A4. Moreover, the calculated binding free energies were found to be in good agreement with the values predicted from a simple 2-ligand binding kinetic model as well as to successfully reproduce the experimental titration curve. This confirms the general applicability of rapid free-energy methods to study challenging biomolecular systems like cytochromes P450, which are characterized by a large flexibility and malleability of their active sites.
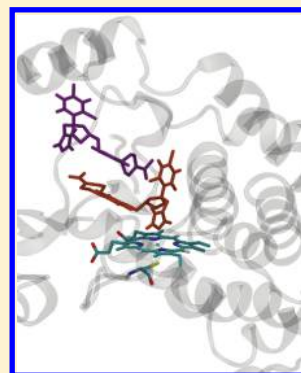
1. INTRODUCTION

Cytochromes P450 (CYPs) constitute a large family of heme-containing enzymes that are found in virtually all organisms.[1] They function as monooxygenases and play a central role in the metabolism of endogenous compounds and xenobiotics.[2] This family shares a common structural feature—a planar ferric-protoporphyrin IX heme complex, which is on the proximal side linked to the protein through a ligated thiolate group of the conserved cystein residue.

Among 57 human isoforms cytochrome P450 3A4 (CYP3A4) represents the most abundant one and is primarily expressed in hepatic tissue and in the small intestine.[3] CYP3A4 is extremely promiscuous and metabolizes more than 50% of clinically used drugs. It is also the isoform most often involved in adverse drug–drug interactions, it activates chemical carcinogens like aflatoxins or tamoxifen and is consequently of immense interest to medicinal chemists.[4] Therefore, it might prove highly beneficial to inhibit CYP3A4 action in cases of acute aflatoxin poisoning while simultaneously inducing the enzymes involved in detoxification and elimination of xenobiotics like glutathione S-transferases, UDP-glucuronosyl transferases, and NAD(P)H:quinone reductase.[5]

CYP3A4 displays atypical binding and kinetic behavior toward a number of ligands characterized by a sigmoidal shape of the corresponding titration curves, which is indicative of a positive homotropic cooperativity.[6,7] This requires a participation of at least two ligand molecules, whereby the binding of the first ligand molecule increases the affinity of CYP3A4 for the binding of the second ligand molecule. However, the observed CYP3A4 cooperativity differs from common allosteric regulation in the sense that it is attributed to simultaneous occupancy of a single active site by multiple ligand molecules. Consequently, its mechanistic origin is poorly understood and involves a direct interaction between the bound ligand molecules and/or selecting and locking a specific preexisting conformation of CYP3A4 with a higher affinity for the second ligand molecule.

The antifungal drug ketoconazole is a well established CYP3A4 inhibitor giving rise to a type II shift in the heme Soret spectrum, indicative of distal-side heme-iron coordination by a nitrogen atom in the inhibitor.[8,9] Ketoconazole binding was found to exhibit positive homotropic cooperativity[10] and a

crystal structure of CYP3A4 with two ketoconazole molecules occupying the active site (PDB code 2V0M)[11] was also obtained. This structure displays one ketoconazole molecule coordinating the heme-iron with its imidazole group, which we will designate inhibitor I, and an additional ketoconazole molecule stacked in an antiparallel orientation above the previous one, to be called inhibitor II. The chemical structure of ketoconazole and a representation of the CYP3A4 active site in complex with both inhibitors are depicted in Figure 1.
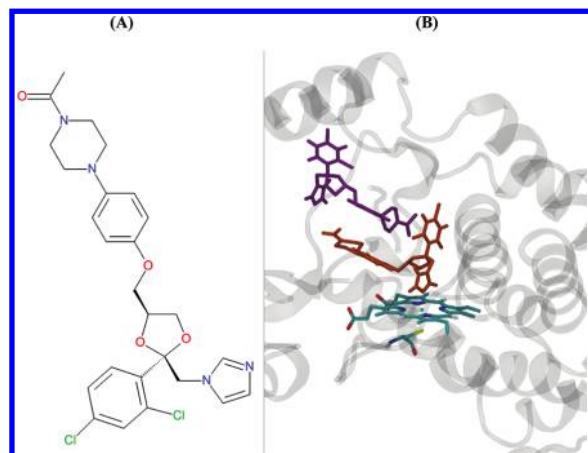

Figure 1. (A) Chemical structure of ketoconazole. (B) Structure of the CYP3A4 active site in complex with two ketoconazole molecules. The heme group and the proximal cystein 422 are colored according to atom types (carbon in cyan, oxygen in red, nitrogen in blue, hydrogen in white, iron in green, and sulfur in yellow), the ketoconazole molecule coordinating the distal side of the heme-iron with its imidazole nitrogen atom (inhibitor I) is in orange, and the second stacked ketoconazole molecule (inhibitor II) is in magenta.

In the present study, we apply molecular dynamics (MD) simulations in conjunction with free-energy calculations to discern the physical origin of positive homotropic cooperativity in ketoconazole binding to CYP3A4. The relatively large active site of CYP3A4 shows large flexibility (allowing for side chain fluctuations and the presentation of various functional groups) as well as a large malleability (the ability to take on a different shape depending on the ligand), which make it a challenging protein to simulate.[12] Simulations of systems involving CYP3A4, CYP3A4 in complex with inhibitor I, CYP3A4 in complex with inhibitor II, and CYP3A4 in complex with both inhibitors were carefully compared in terms of structural and energetic properties. Clearly, a deeper mechanistic understanding of CYP3A4 cooperative binding is indispensible to rationalize and predict ligand–CYP interactions and related adverse drug–drug effects, making it a fundamental question of both scientific and pharmaceutical importance.

2. METHODS

2.1. Free-Energy Calculations. The Linear Interaction Energy (LIE) method of Åqvist and co-workers[13] represents a rapid approach of evaluating solvation free energies. It is based on a modified linear response to treat electrostatic interactions and on an empirical term treating the dispersion interactions. A term describing the hydrophobic interactions can potentially be added.[14] The solvation free energy $\Delta G_{solv}^{L(S)}$ of a solute L in a surrounding solvent S is expressed as

$$\Delta G_{solv}^{L(S)} = \alpha \langle V_{vdW}^{L(S)} \rangle_Q + \beta \langle V_{es}^{L(S)} \rangle_Q + \gamma^{L(S)} \tag{1}$$

where $\langle V_{vdW}^{L(S)} \rangle_Q$ and $\langle V_{es}^{L(S)} \rangle_Q$ represent van der Waals and electrostatic interaction energy between the solute L and its surrounding solvent S, respectively, averaged over an ensemble of configurations generated by MD simulation. The subscript Q indicates that this ensemble is obtained with the regular partial charges of the solute. α, β, and $\gamma^{L(S)}$ are coefficients of the LIE method, where β has the theoretical value of 0.5. In practice, α, β, and possibly $\gamma^{L(S)}$ are often determined empirically.[13,14] This approach directly yields contributions to $\Delta G_{solv}^{L(S)}$ due to dispersion, electrostatic, and hydrophobic interactions. In addition, if the interaction energy V can be additively decomposed into atom-group contributions, the resulting solvation free energy can readily be interpreted in terms of interactions between specific groups of atoms in the system.[15,16]

The Linear Response Approximation (LRA) method of Warshel and co-workers[17] represents an alternative rapid approach to evaluate solvation free energies. It is based on a linear response to treat electrostatic interactions and on an empirical term treating the dispersion interactions. The solvation free energy $\Delta G_{solv}^{L(S)}$ of a solute L in a surrounding solvent S is expressed as

$$\Delta G_{solv}^{L(S)} = \alpha \langle V_{vdW}^{L(S)} \rangle_Q + \beta \langle V_{es}^{L(S)} \rangle_Q + \beta \langle V_{es}^{L(S)} \rangle_0 \tag{2}$$

where $\langle V_{vdW}^{L(S)} \rangle_Q$ and $\langle V_{es}^{L(S)} \rangle_Q$ are defined as before and $\langle V_{es}^{L(S)} \rangle_0$ represents the average electrostatic interaction energy between the solute L and its surrounding solvent S calculated over an ensemble of configurations generated by MD simulation using a solute L in which all partial charges have been set to zero. As in LIE, β has a theoretical value of 0.5, while α is determined empirically. The individual terms in eq 2 are associated with contributions from dispersion and electrostatic interactions as well as with an electrostatic preorganization contribution to the calculated solvation free energy. Again, the contributions from specific atom-group interactions are readily identified.[15,16]

Preorganized electrostatics ($\beta \langle V_{es}^{L(S)} \rangle_0$) reflects the electrostatic interaction of a solute with its preorganized environment, the geometry and polarization of which is established in the presence of zero partial charges on all solute atoms.[18] If solute L with all partial atomic charges set to zero is immersed in water, the solvent dipoles are randomly oriented with respect to it. If the water and the solute geometries remain unchanged during the charging process of the solute (i.e., if this process was instantaneous), the overall charge dipole interaction energy is zero ($\langle V_{es}^{L(S)} \rangle_0 = 0$). Thus, we can say that polar solvents are not electrostatically preorganized to accommodate solute molecules. On the other hand, in proteins the binding site dipoles associated with polar groups and ionized residues may be already partially oriented toward the bound ligand L with all partial atomic charges set to zero. The analogous instantaneous charging of the bound ligand may therefore yield favorable electrostatic interactions between the protein and its ligand ($\langle V_{es}^{L(S)} \rangle_0 < 0$), in which case one can claim that proteins are electrostatically preorganized to accommodate their ligands. The electrostatic preorganization represents the main source of the catalytic power of many enzymes.[19] Its origin can be traced to the process of protein folding, whereby the protein attains its 3D structure and its dipoles get oriented.[20]

Cooperativity of ketoconazole binding to CYP3A4 was studied with the help of the thermodynamic cycle presented in
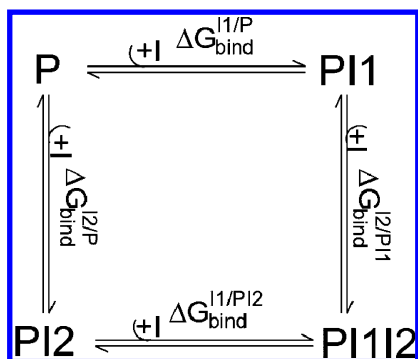
Figure 2. Thermodynamic cycle to study cooperative ketoconazole binding to CYP3A4. Apo CYP3A4 is presented by P, doubly ligated CYP3A4, by PI1I2, CYP3A4 in complex with inhibitor I, by PI1, and CYP3A4 in complex with inhibitor II, by PI2.

Figure 2. Doubly ligated CYP3A4 (PI1I2) can be obtained from the apo CYP3A4 (P) by the binding of the first ketoconazole molecule at the position of inhibitor I leading to formation of a monoligated CYP3A4 (PI1) followed by the binding of the second ketoconazole molecule at the position of inhibitor II. The free energy of the initial binding $\Delta G_{bind}^{I1/P}$ can be calculated as a difference between the solvation free energies of ketoconazole at the position of inhibitor I in the apo CYP3A4, $\Delta G_{solv}^{I1(P)}$, and of ketoconazole in aqueous solution, $\Delta G_{solv}^{I(W)}$:[13,17,21]

$$\Delta G_{bind}^{I1/P} = \Delta G_{solv}^{I1(P)} - \Delta G_{solv}^{I(W)} \qquad (3)$$

The free energy of the subsequent binding $\Delta G_{bind}^{I2/PI1}$ can be calculated as a difference between the solvation free energies of ketoconazole at the position of inhibitor II in a monoligated CYP3A4, $\Delta G_{solv}^{I2(PI1)}$, and of ketoconazole in aqueous solution, $\Delta G_{solv}^{I(W)}$. A correction for the altered solvation of inhibitor I upon the transition from mono to doubly ligated CYP3A4 also needs to be added to ensure cycle closure in Figure 1:

$$\Delta G_{bind}^{I2/PI1} = \Delta G_{solv}^{I2(PI1)} - \Delta G_{solv}^{I(W)} + \Delta G_{solv}^{I1(PI2)} - \Delta G_{solv}^{I1(P)} \qquad (4)$$

Alternatively, doubly ligated CYP3A4 (PI1I2) can also be obtained from the apo CYP3A4 (P) by the binding of the first ketoconazole molecule at the position of inhibitor II leading to formation of a monoligated CYP3A4 (PI2) followed by the binding of the second ketoconazole molecule at the position of inhibitor I. The corresponding free energies $\Delta G_{bind}^{I2/P}$ and $\Delta G_{bind}^{I1/PI2}$ are defined analogously as

$$\Delta G_{bind}^{I2/P} = \Delta G_{solv}^{I2(P)} - \Delta G_{solv}^{I(W)} \qquad (5)$$

$$\Delta G_{bind}^{I1/PI2} = \Delta G_{solv}^{I1(PI2)} - \Delta G_{solv}^{I(W)} + \Delta G_{solv}^{I2(PI1)} - \Delta G_{solv}^{I2(P)} \qquad (6)$$

The free energy along the thermodynamic cycle depicted in Figure 2 can be expressed:

$$\Delta G_{cyc} = \Delta G_{bind}^{I1/P} + \Delta G_{bind}^{I2/PI1} - \Delta G_{bind}^{I1/PI2} - \Delta G_{bind}^{I2/P} \qquad (7)$$

Using eqs 3–6, ΔG_{cyc} evaluates to zero exactly, as is appropriate for a state function.

2.2. Preparation of Initial Structures. The crystal structure of CYP3A4 in complex with two ketoconazole molecules (PDB code 2V0M)[11] served as a starting point. In this structure, the asymmetric unit cell consists of four copies of the enzyme of which the N-terminal transmembrane helix was truncated to allow for crystallization. Monomer A was selected based on the good resolution of both inhibitor molecules. Coordinates for the missing loops Thr-264 to Arg-268 and Asn-280 to Lys-288 were obtained from monomer C. Missing side-chain atoms of Lys-168, His-287, and Asp-497 were manually added. All Lys, Arg, and Cys (with exception of proximal Cys-442) side-chains were protonated; all Asp and Glu side-chains were deprotonated; the amino and carboxy termini were charged; the His-65 side-chain was charged; the His-30 side-chain was N_ε-protonated; and all other His side-chains were N_δ-protonated based on visual inspection of hydrogen bonding networks. This procedure yielded the initial structure of the PI1I2 system. Initial structures of four additional systems were subsequently generated: PI1 by deletion of inhibitor II, PI2 by deletion of inhibitor I, P by deletion of both inhibitors, and W by deletion of the enzyme and inhibitor II.

2.3. Simulation Setup. All simulations were performed and analyzed using the GROMOS11 simulation package.[22] The GROMOS 45A4 force field was applied. Ketoconazole interaction parameters were manually selected based on analogy with similar groups represented in the GROMOS 45A4 force field and are available in the Supporting Information. The Heme group was represented by the default GROMOS parameters with the Fe^{2+} ion covalently bound to Cys422. No sixth ligand was covalently linked to the Fe^{2+} ion. The five studied systems were energy-minimized and placed into a periodic pre-equilibrated rectangular box of SPC water.[23] Minimum solute to solvent and minimum solute to box-wall distances were set to 0.23 and 0.8 nm, respectively. Water molecules were energy-minimized using the steepest-descent algorithm. Subsequently four of them were selected based on their electrostatic potential and replaced by chloride ions to achieve electroneutrality in systems P, PI1, PI2, and PI1I2.

The following equilibration protocol was used: Initial velocities were randomly generated from a Maxwell–Boltzmann distribution at 50 K. All solute atoms were restrained to their initial positions through a harmonic potential with force constant of 2.5×10^4 kJ mol^{-1} nm^{-2}, and the systems were propagated for 20 ps. In each of the five subsequent 20 ps MD simulations, the temperature was raised by 50 K and the positional restraints were reduced by 1 order of magnitude. Then, positional restraints were removed, roto-translational constraints on all solute atoms were introduced,[24] and the systems were simulated for 20 ps at 300 K. Finally, a simulation at a constant pressure of 1 atm was performed for 300 ps.

Production runs of 10 ns at 300 K and atmospheric pressure followed. System coordinates and energies were stored every 0.5 ps for further analysis. Temperature and pressure were kept constant using the weak coupling scheme[25] with relaxation times of 0.1 and 0.5 ps, respectively. Separate temperature baths were used for solute and solvent and an isothermal compressibility of 4.575×10^{-4} kJ^{-1} mol nm^3 was applied. Bond lengths were constrained using the SHAKE algorithm[26] allowing for time steps of 2 fs. Nonbonded interactions were calculated using a triple range scheme. Interactions within a short-range cutoff of 0.8 nm were calculated every step from a pairlist that was updated every fifth step. At these points, interactions between 0.8 and 1.4 nm were also calculated and kept constant between updates. A reaction field[27] contribution was added to the electrostatic interactions and forces to account for a homogeneous medium outside the long-range cutoff using

a relative dielectric constant of 61 as appropriate for the SPC water model.[28]

300 ps equilibration simulations involving inhibitors with all partial charges set to zero were initiated from the equilibrated systems. Subsequent production simulations of 4 ns at 300 K and 1 atm were analyzed in terms of preorganized electrostatics.

3. RESULTS AND DISCUSSION

3.1. Structure of CYP3A4. During 10 ns MD simulations, the root-mean-square deviation (rmsd) of the CYP3A4 backbone atoms with respect to their initial crystal structure configuration settles at values reported in Table 1. The

Table 1. Final RMSD of the CYP3A4 Backbone Atoms with Respect to Their Initial Crystal Structure Configuration and an Average Active-Site Volume Obtained during 10 ns MD Simulations of the Four Studied CYP3A4 Systems

system	rmsd [nm]	active-site volume [nm^3]
P	0.32	3.8 ± 0.9
PI1	0.31	2.0 ± 0.1
PI2	0.21	2.3 ± 0.2
PI1I2	0.24	2.6 ± 0.1

presence of inhibitor II seems to be responsible for maintaining CYP3A4 conformation close to its crystal structure. This statement can be further corroborated by the slight decrease of the rmsd of the CYP3A4 backbone atoms in the PI2 system with respect to their final structure in the PI1I2 system from 0.26 to 0.23 nm during the course of the 10 ns MD simulation. This is the only pair of studied systems that exhibits such structural convergence. The simulated rmsd values are of greater magnitude than the backbone rmsd of our initial structure with respect to the two existing human apo CYP3A4 crystal structures (1TQN[29] of 0.18 nm and 1W0E[30] of 0.16 nm), or with respect to the four monoligated human CYP3A4 crystal structures in complex with progesterone (1W0F[30] of 0.17 nm), metyrapone (1W0G[30] of 0.18 nm), erythromycin A (2J0D[11] of 0.18 nm), and ritonavir (3NXU[9] of 0.07 nm). Therefore, the CYP3A4 conformational space explored by the means of MD simulations seems to be larger than the one covered by the current crystallographic data. On the other hand, the simulated conformational space is still relatively confined and the largest backbone rmsd value is observed between the final structures of simulated systems P and PI1 at 0.37 nm.

Root-mean-square fluctuations (RMSF) of the CYP3A4 backbone were calculated over the 10 ns MD simulations and are collected in Figure 3. Like expected, both the N- and C-termini as well as the modeled loops Thr-264 to Arg-268 and Asn-280 to Lys-288 exhibit large fluctuations in all simulated systems. All remaining regions of high RMSF (Arg-105 to Gly-109, Arg-161 to Lys-169, Asp-194 to Gln-200, Lys-342 to Thr-346, and Glu-417 to Asp-428) can be assigned to flexible solvent-exposed loops of CYP3A4. Significant fluctuations of the Phe-219 to Thr-224 region are observed in the PI1 system only, which can probably be attributed to the loss of a stabilizing hydrogen bond between the imidazole nitrogen of inhibitor II and the hydroxyl group of Thr-224. All in all, systems PI1I2 and PI2 exhibit smaller fluctuations of the CYP3A4 backbone than systems PI1 and P, which again suggests the presence of inhibitor II as the key element for maintaining the CYP3A4 conformation close to the initial
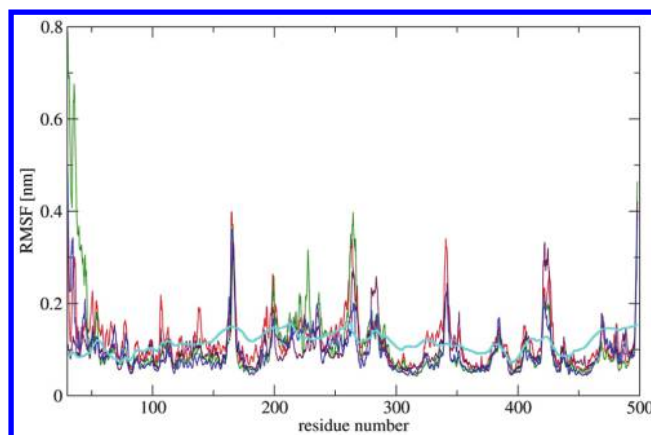

Figure 3. Root-mean-square fluctuations (RMSF) of the CYP3A4 backbone observed for the apo protein (P in red) and the three studied complexes (PI1 in green; PI2 in maroon; PI1I2 in blue) during the course of 10 ns MD simulations. RMSF values calculated from the crystal-structure B-factor values are depicted in cyan.

crystal structure. Finally, good qualitative agreement between the simulated CYP3A4 backbone RMSF and the RMSF calculated from the crystal-structure B-factor values should be noted.

Since the studied systems differ in the occupancy of the CYP3A4 active site, the volume of the cavity at the distal side of the heme was monitored using the CASTp server;[31] see Table 1. The active site exhibits comparable though somewhat larger flexibility than the rest of the protein. The apo CYP3A4 cavity seems extremely malleable[32] and opens up to 3.8 ± 0.9 nm^3, which is quite similar to the cavity volume of 3.7 nm^3 observed in the crystal structure with bound erythromycin A even though apo crystal structures 1TQN[29] and 1WE0[30] show significantly smaller active-site volumes of 1.9 and 1.7 nm^3, respectively. The changes in the CYP3A4 active-site volume and structure for systems P, PI1, and PI2 are depicted in Supporting Information Figure 1.

On average, one ketoconazole molecule is in the monoligated systems PI1 and PI2 replaced by 15 ± 8 (average ± standard deviation) water molecules. In the apo system, both ketoconazole molecules are replaced by 45 ± 11 water molecules. The water ingress channels[33] remain open and 83 ± 5% of the water molecules experience exchange with bulk solvent during the course of 10 ns MD simulations. A water molecule was in the P system observed within 0.3 nm from the heme iron for 21% of the simulation time. As no covalent link was included, this represents a coordination through non-bonded interactions. About 15 different water molecules were involved in this coordination.

The evolution of the CYP3A4 secondary-structure elements during the simulations is compared in Supporting Information Figure 2. In PI1I2 the secondary structure remains stable with the exception of a partial unwinding of the short N-terminal α-helix, of the two short helices preceding the L α-helix, and of the short 3-1 β-strand. PI2 behaves very similarly, again indicating the importance of inhibitor II for the preservation of the initial secondary structure of CYP3A4. On the other hand, PI1 system experiences partial unwinding of the short helix preceding the A α-helix and of the short helix following the B α-helix as well. Simultaneously, the short 3-1 β-strand gets reinforced. The largest structural deviations are, however, observed in the apo CYP3A4 with the partial unwinding of the

Table 2. Average Ligand–Water $\langle V_{vdW}^{L-W}\rangle_Q$ and Ligand–Protein $\langle V_{vdW}^{L-P}\rangle_Q$ van der Waals Interaction Energies, Average Ligand–Water $\langle V_{es}^{L-W}\rangle_Q$ and Ligand–Protein $\langle V_{es}^{L-P}\rangle_Q$ Electrostatic Interaction Energies, and Average Intramolecular $\langle V^{L-L}\rangle_Q$ Ligand Interaction Energies As Well As Schlitter $S_{Schlitter}^L$ and Quasiharmonic $S_{Quasiharmonic}^L$ Ligand Configurational Entropies Collected from MD Simulations in Water and in the Three Studied Complexes[a]

ligand	system	$\langle V_{es}^{L-W}\rangle_Q$	$\langle V_{vdW}^{L-W}\rangle_Q$	$\langle V_{es}^{L-P}\rangle_Q$	$\langle V_{vdW}^{L-P}\rangle_Q$	$\langle V^{L-L}\rangle_Q$	$S_{Schlitter}^L$	$S_{Quasiharmonic}^L$
				kJ mol^{-1}			J mol^{-1} K^{-1}	
I	W	−111 ± 1	−185 ± 1			211.6	1209	1154
I1	PI1	9 ± 1	−33 ± 2	−95 ± 2	−294 ± 3	180.4(−31.1)	750(−459)	702(−452)
I2	PI2	−64 ± 2	−48 ± 2	−15 ± 2	−249 ± 4	188.3(−23.3)	1053(−156)	1004(−150)
I1	PI1I2	−16 ± 1	−22 ± 2	−27 ± 1	−256 ± 1	176.9(−34.7)	781(−428)	732(−422)
I2	PI1I2	−12 ± 2	−28 ± 1	−104 ± 4	−236 ± 3	186.2(−25.4)	916(−293)	866(−288)

[a]The change in configurational entropy and intramolecular interaction energy upon ligand binding is reported in parentheses. Error estimates are obtained from block averaging and subsequent extrapolation to infinite block lengths.[51]

D, I, and J α-helices and with the complete loss of the short 3-1 β-strand.

3.2. Important Interactions, Configurational Entropy, and Conformational Clustering of Inhibitors. The presence of hydrogen bonds was monitored over the simulations using a geometric criterion. A hydrogen bond is considered to be formed if the distance between the hydrogen and acceptor atoms is less than 0.25 nm and the donor–hydrogen–acceptor angle is larger than 135°. The hydrogen bond between the keto group of inhibitor I and the side chain of Arg-372, which is observed in the original crystal structure,[11] is present for more than 90% of the time in the monoligated PI1 system simulation. The imidazole nitrogen of inhibitor I coordinates the heme iron tightly at an average distance of 0.26 nm. In 40% of the snapshots, it also forms a hydrogen bond to the side chain of the conserved Thr-309 from the I α-helix. An additional hydrogen bond between the phenolic-ether oxygen of inhibitor I and the side chain of Arg-105 was observed for 70% of the time as well. In this light it is easy to understand why inhibitor I possesses very favorable average electrostatic interaction energies with the surrounding protein, reported in Table 2. On the basis of the average van der Waals interaction energies, inhibitor I is also very well embedded in the CYP3A4 active site. Consequently, the atoms of inhibitor I in the monoligated PI1 system exhibit the lowest root-mean-square fluctuations depicted in Figure 4 and give rise to the smallest

Figure 4. Root-mean-square fluctuations (RMSF) of the ketoconazole inhibitor atoms observed in water (red curve) and in the three studied complexes (I1 in PI1 in green; I1 in PI1I2 in magenta; I2 in PI2 in blue; I2 in PI1I2 in yellow) during the course of 10 ns MD simulations.

configurational entropy calculated by either the Schlitter[34] or the quasiharmonic[35] approach (Table 2). The configurational entropy represents only a part of the complete entropy, but provides insight into the conformational restriction due to the protein environment.

The hydrogen-bonded interaction between the keto group of inhibitor I and the side-chain of Arg-372 becomes water-mediated in the doubly ligated PI1I2 system simulation. The imidazole nitrogen of inhibitor I coordinates the heme-iron tightly at an average distance of 0.24 nm, but the hydrogen bonds with Thr-309 and Arg-105 are lost. Consequently, the average electrostatic interaction energies of inhibitor I are significantly weakened and almost equally distributed between water and protein (Table 2). The atoms of inhibitor I in the doubly ligated PI1I2 system also exhibit larger root-mean-square fluctuations (Figure 4) and show a bigger configurational entropy (Table 2). However, based on the average van der Waals interaction energies (Table 2), inhibitor I is still very well embedded in the CYP3A4 active site.

The hydrogen bond between the keto group of inhibitor II and the side-chain of Ser-119, which is observed in the original crystal structure,[11] is present for more than 98% of the time in the doubly ligated PI1I2 system simulation. The imidazole nitrogen of inhibitor II is hydrogen-bonded to the side chains of Arg-106 and Thr-224. It is interesting to note that by means of MD simulations both Ser-119 and Arg-106 have also been identified as key residues for progesterone binding.[36] Consequently, inhibitor I possesses very favorable average electrostatic interaction energies with the surrounding protein (Table 2). However, based on the average van der Waals interaction energies (Table 2), inhibitor II is to a lesser extent embedded in the doubly ligated CYP3A4 active site, which is in agreement with larger root-mean-square fluctuations (Figure 4) and a larger configurational entropy (Table 2).

The hydrogen-bonded interactions between the keto group of inhibitor II and the side chain of Ser-119 and between the imidazole nitrogen of inhibitor II and the side chain of Arg-106 become water-mediated in the monoligated PI2 system simulation. Correspondingly, the average electrostatic interaction energies of inhibitor II are significantly weakened and mainly originate from the surrounding water (Table 2). On the basis of the average van der Waals interaction energies (Table 2), inhibitor II is not so firmly embedded in the monoligated CYP3A4 active site either. Therefore, largest root-mean-square fluctuations (Figure 4) and the largest configurational entropy (Table 2) of all bound ketoconazole molecules was observed in this simulation. It is also interesting to note that the keto group of inhibitor II starts to interact with the side chain of Phe-304,
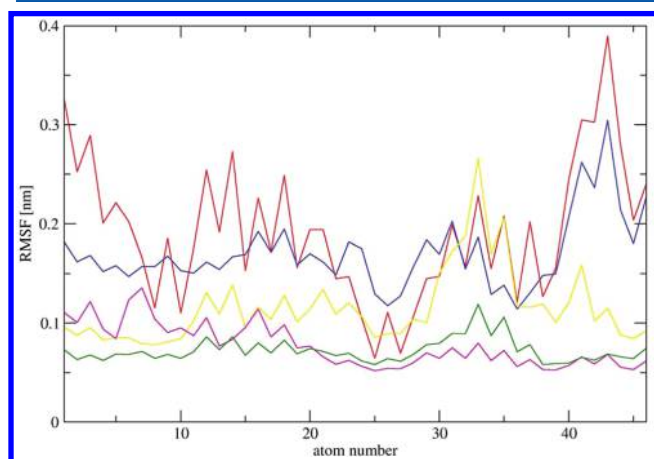
1577

dx.doi.org/10.1021/ci300118x | J. Chem. Inf. Model. 2012, 52, 1573–1582

which has been identified by means of MD simulations as influencing the cooperative behavior of diazepam binding to CYP3A4 through stacking interactions.[37]

In the doubly ligated PI1I2 system the two antiparallel ketoconazole molecules interact favorably mainly through an attractive van der Waals interaction energy of an average -54 ± 1 kJ mol^{-1}. Hydrogen-bonded interactions between the two do not exist leading to an average electrostatic interaction energy of -4 ± 1 kJ mol^{-1}. Ketoconazole in water (state W) exhibits the largest root-mean-square fluctuations (Figure 4) yielding the largest configurational entropy (Table 2). The decrease in configurational entropy upon inhibitor binding indicates that the process is entropically unfavorable from the standpoint of ketoconazole (Table 2). It is important to note that, although the Schlitter and quasiharmonic approaches provide different absolute values of configurational entropy, they yield almost identical changes in configurational entropy upon inhibitor binding due to their intrinsic dependence on the harmonic analysis.[38−40] Unfortunately, the entropic contributions of the protein and the displaced water molecules cannot be accurately calculated from these simulations which precludes any meaningful comparison with the experimental binding entropy.[41]

During 10 ns MD simulations the root-mean-square deviation (rmsd) of inhibitor I atoms with respect to their initial crystal structure configuration after a rotational fit based on the backbone atoms of CYP3A4 settles at 0.19 nm for the monoligated system PI1 and at 0.17 nm for the doubly ligated system PI1I2. The structure of inhibitor I in the two systems slightly diverges during the course of the MD simulation to 0.22 nm with respect to each other. Using the identical procedure the rmsd of inhibitor II atoms with respect to their initial crystal structure configuration settles at somewhat higher values of 0.29 nm in the monoligated system PI2 and at 0.23 nm in the doubly ligated system PI1I2. The structure of inhibitor II in the two systems slightly converges during the course of the MD simulation from a rmsd value of 0.34 to 0.28 nm, which may help to explain how the presence of inhibitor II is capable of enforcing a specific conformation (close to the initial crystal structure) onto CYP3A4.

20 000 ketoconazole structures were collected from the water system (W) production run at 0.5 ps intervals along with 5000 ketoconazole structures from each of the four (inhibitor I in system PI1, inhibitor II in system PI2, inhibitor I in system PI1I2, and inhibitor II in system PI1I2) CYP3A4-bound ketoconazole production runs at 2 ps intervals, and the rmsd was after a rotational fit to remove the translational and rotational motion calculated between all pairs of structures. Pairs of ketoconazole structures with rmsd values smaller than 0.2 nm were considered structural neighbors, and the structure with the largest number of neighbors was considered the central member of a first cluster.[42] After removing all structures belonging to this first cluster, the procedure was iteratively repeated until no structure was left and 22 clusters were formed. The population of the six largest clusters with overall more than 1000 structures is depicted in Figure 5, and the corresponding central members are presented in Supporting Information Figure 3. All clusters include ketoconazole structures obtained from the water simulation, whereas only certain clusters additionally include CYP3A4-bound ketoconazole structures. Therefore, each simulated CYP3A4 system is capable of binding only selected ketoconazole structures from the preexisting water-phase ensemble of ketoconazole con-
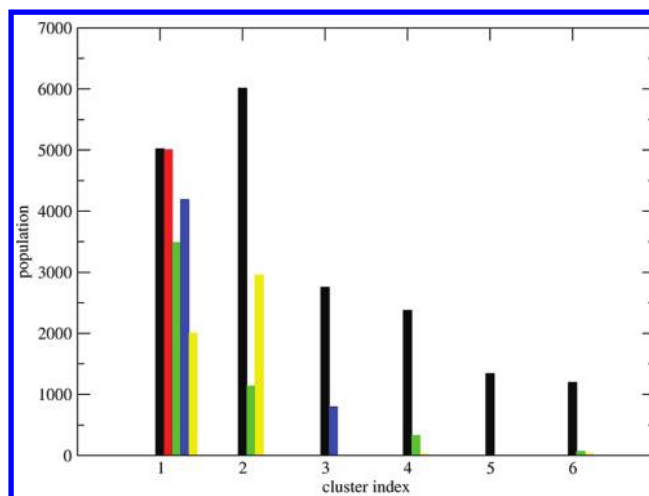

Figure 5. Population of the six largest clusters with more than 1000 ketoconazole structures obtained from clustering 20 000 snapshots from the water production run (black bars) and 5000 from the three simulated CYP3A4 complexes each (I1 in PI1 in red; I1 in PI1I2 in blue; I2 in PI2 in green; I2 in PI1I2 in yellow).

formations thereby confirming the conformational selection mechanism[43] at least from the standpoint of the inhibitor. In addition, the lower flexibility of the ketoconazole molecule bound in the position of inhibitor I is reflected by its occurrence in clusters 1 and 3 only.

The average intramolecular interaction energies consisting of electrostatic, van der Waals, and covalent contributions represent the last missing piece of information on the binding behavior of ketoconazole. Somewhat counterintuitively, intramolecular interactions become more favorable upon ketoconazole binding to CYP3A4 (Table 2) with energy differences stemming mainly from covalent contributions. This finding was confirmed by the cluster analysis (Figure 5). The covalent interaction energy of the central member of cluster 1, which includes a large majority of all bound ketoconazole structures, evaluates to 118 kJ mol^{-1}. On the other hand, the covalent interaction energy is significantly larger in the case of the central members of clusters 2, which includes most of unbound ketoconazole structures, and 5, which includes only unbound ketoconazole structures, totalling 161 and 154 kJ mol^{-1}, respectively. These differences originate from a number of angles, dihedral angles, and improper dihedrals—all of which involve polar atom groups, whose respective geometries deviate from the optimal ones presumably due to favorable electrostatic interactions with the neighboring water molecules. In the bound state, CYP3A4 seems not to enforce such perturbations of the ketoconazole structure which can be perceived as yet another manifestation of its active-site malleability.

Finally, a 10 ns MD simulation of a hydrated ketoconazole dimer in the antiparallel orientation was performed to check for its stability. The structure was found to collapse within the first 3 ns.

3.3. Binding Affinities. The average electrostatic and van der Waals interaction energies of ketoconazole in water as well as in the three studied complexes are reported in Table 3. From the size of the binding energies we conclude that shape complementarity through nonpolar van der Waals interactions represents the main driving force of ketoconazole binding. Taken together with the large size of the active site, its flexibility, and malleability, this has the potential to explain why

1578

dx.doi.org/10.1021/ci300118x | J. Chem. Inf. Model. 2012, 52, 1573−1582

Table 3. Average Electrostatic $\langle V_{es}^{L(S)} \rangle_Q$ **and van der Waals** $\langle V_{vdW}^{L(S)} \rangle_Q$ **Interaction Energy between Solute L and Its Surrounding S, Respectively, Sampled on the Charged State of Solute L As Well As the Corresponding Average Electrostatic Interaction Energy** $\langle V_{es}^{L(S)} \rangle_0$ **Sampled on the Uncharged State of Solute L**[a]

solute	surrounding	$\langle V_{es}^{L(S)} \rangle_Q$	$\langle V_{vdW}^{L(S)} \rangle_Q$	$\langle V_{es}^{L(S)} \rangle_0$
		kJ mol^{-1}		
I	W	−111 ± 1	−185 ± 1	0.2 ± 1.3[b]
I1	P	−86 ± 2	−327 ± 1	−17 ± 1
I2	P	−80 ± 3	−297 ± 2	−4 ± 2
I1	PI2	−47 ± 1	−333 ± 1	−15 ± 1
I2	PI1	−121 ± 3	−318 ± 3	−3 ± 2

[a]Values are averaged over MD simulations of ketoconazole in water and in the three studied complexes. Error estimates are obtained from block averaging and subsequent extrapolation to infinite block lengths.[51] [b]The theoretically expected value of 0 was used instead in all subsequent calculations.

CYP3A4 is extremely promiscuous.[3] On the other hand, only inhibitor II of the doubly ligated CYP3A4 exhibits more favorable electrostatic interactions than the free ketoconazole. However, this does not mean that electrostatic interactions do not play a role in ketoconazole binding to CYP3A4. In fact, several hydrogen bonds and other polar contacts were detected with various active-site residues and water molecules, which facilitate a proper orientation of ketoconazole inhibitors in the binding pocket. The weakening of the electrostatic interactions in the remaining three cases merely indicates a small decrease in the average number of ketoconazole polar contacts upon its transfer from the water solution to the CYP3A4 active site, which can be easily compensated by the more favorable nonpolar interactions. Very similar behavior was observed in the case of CYP1A2, for which LIE empirical parameters were optimized based on a set of 13 ligands.[44] Consequently, this LIE model was also introduced to the current study of ketoconazole binding to CYP3A4 and labeled as model LIE0— the resulting binding free energies are reported in Table 4.

Binding of ketoconazole to the apo structure of CYP3A4 in the position of inhibitor II is the weakest, binding to the monoligated CYP3A4 in the position of inhibitor I is the strongest, and binding to the apo CYP3A4 in the position of inhibitor I or to the monoligated CYP3A4 in the position of inhibitor II are of similar intermediate affinity. Ketoconazole binding to the monoligated CYP3A4 is 5 kJ mol^{-1} stronger than ketoconazole binding to the apo CYP3A4 for both positions. Therefore, the binding of the initial ketoconazole molecule increases the affinity for the binding of the second ketoconazole molecule by 5 kJ mol^{-1}, which explains and

quantifies the experimentally observed positive homotropic cooperativity of CYP3A4.[10] Shape complementarity through nonpolar van der Waals interactions represents the sole molecular origin of this phenomenon.

Figure 6 depicts how the constitution of a reaction mixture containing 1 μM of CYP3A4 changes with increasing
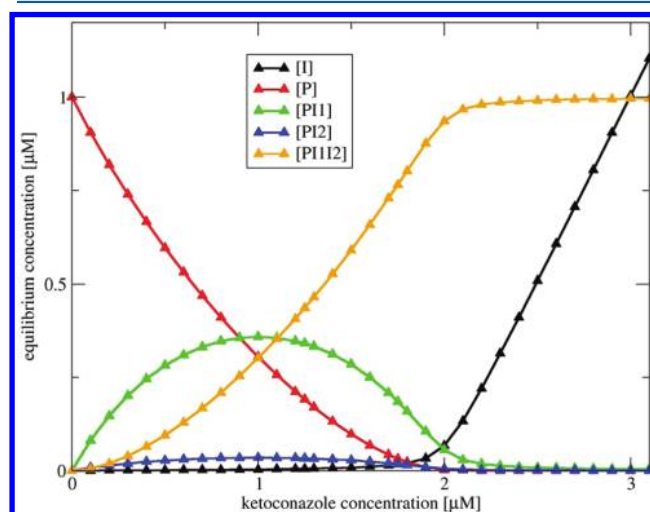

Figure 6. Constitution of the reaction mixture containing 1 μM of CYP3A4 as a function of the ketoconazole concentration according to the binding free energies predicted using the LIE0 model.

ketoconazole concentration according to the binding free energies predicted with the LIE0 model. The presence of apo CYP3A4 (P) decreases with increasing ketoconazole concentration and represents the most abundant species for ketoconazole concentrations below 0.9 μM. The presence of doubly ligated CYP3A4 (PI1I2) increases with increasing ketoconazole concentration and represents the most abundant species for ketoconazole concentrations above 1.2 μM. The presence of monoligated PI1 and PI2 exhibits a maximum in the intermediate ketoconazole concentration range—PI1 represents the most abundant form while the concentration of PI2 never exceeds 0.04 μM. Note that formation of the PI1I2 complex via the PI2 intermediate is sterically hindered. However, this does not imply that PI2 does not occur at all.

A simple two-ligand binding model leading to the formation of monoligated (PI1) and doubly ligated (PI1I2) CYP3A4— both causing an identical absorbance change in the heme Soret spectra—was proposed earlier and experimentally verified on the ketoconazole binding kinetic data.[10] A dissociation constant of 0.007 μM was obtained for the monoligated PI1 species, corresponding to an experimental binding free energy of −47 kJ

Table 4. Ketoconazole Binding Free Energies Calculated According to Different Computational Models

model	parameters			$\Delta G_{bind}^{I1/P}$	$\Delta G_{bind}^{I2/PI1}$	$\Delta G_{bind}^{I2/P}$	$\Delta G_{bind}^{I1/PI2}$
	α	β	γ[a]	kJ mol^{-1}			
LIE0	0.196	0.014	−21.81	−49.4 ± 0.5	−48.5 ± 0.9	−43.5 ± 0.7	−54.4 ± 0.5
LIE1	0.362	0.035		−50.6 ± 0.8	−49.4 ± 1.4	−39.3 ± 1.2	−60.7 ± 0.8
LRA1	0.375	0.152		−51.9 ± 1.3	−48.1 ± 2.2	−38.1 ± 1.8	−61.9 ± 1.3
LIE2	0.669	1.908		−47.3 ± 7.9	−37.7 ± 9.2	−15.9 ± 8.4	−69.0 ± 7.9
LRA2	0.358	0.432		−47.3 ± 2.4	−37.7 ± 3.5	−28.5 ± 3.2	−56.5 ± 2.4
exp[b]				−47.3	−37.7		

[a]In kJ mol^{-1}. [b]Estimated from a two-step kinetic model.[10]

mol^{-1}, which is in good agreement with the prediction of the LIE0 model for $\Delta G_{bind}^{I1/P}$ of −49.4 kJ mol^{-1}. For the doubly ligated PI1I2 species, a dissociation constant of 0.3 μM was determined yielding an experimental binding free energy of −38 kJ mol^{-1}, which is higher than the prediction of the LIE0 model for $\Delta G_{bind}^{I2/PI1}$ of −48.5 kJ mol^{-1}. A part of the difference can be attributed to the omission of the PI2 species from the simple two-ligand binding kinetic model,[10] which represents a spectroscopically nonproductive mode of binding in the LIE0 model and has to be compensated by a tighter binding of the spectroscopically active PI1 and PI1I2 species. However, the levels of the PI2 species formed are insufficient to explain the entire difference between experimentally observed and computationally predicted binding free energies (Figure 6).

Spectrophotometric equilibrium binding titrations with varying ketoconazole concentrations at fixed final CYP3A4 concentrations of 1 μM have been reported earlier.[10] The
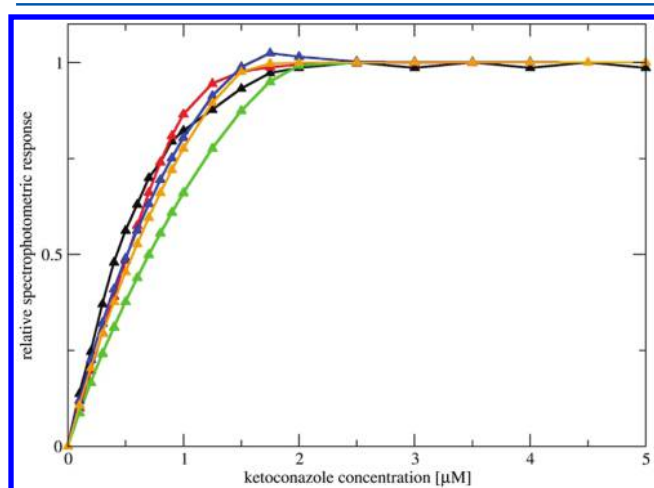

Figure 7. Relative spectrophotometric response of the reaction mixture containing 1 μM of CYP3A4 as a function of the ketoconazole concentration. The experimental data (black curve) and kinetic model (red) are taken from ref 10. Using the affinities of the LIE0 model, the green curve is obtained, which can be adjusted assuming a 40% increased spectroscopic response for PI1 (blue curve) or a 20% decrease in functional CYP3A4 enzymes (yellow).

experimental titration curve depicted in Figure 7 is best fit using the Hill equation

$$\text{RSR} = \frac{c^n}{K^n + c^n} \tag{8}$$

where RSR represents the relative spectrophotometric response and c the total ketoconazole concentration—with a Hill constant K of 0.5 μM and a Hill coefficient n of 2.4. Values of $n > 1.0$ are indicative of a positive homotropic cooperativity.[45] The computational LIE0 model gives a reasonable agreement with the experiment and is best fitted using the Hill equation with a Hill constant K of 0.6 μM and a Hill coefficient n of 2.2. As expected, the simple two-ligand binding model based on the experimental kinetic data yields an even better agreement with the experiment (Figure 7). However, at low ketoconazole concentrations, the experimental titration curve systematically exhibits relative spectrophotometric responses, which are higher than the highest responses theoretically achievable by the simple two-ligand binding

kinetic model (e.g., a relative spectrophotometric response of 48% at a ketoconazole concentration of 0.4 μM—corresponding to 40% of the protein concentration). Consequently, we speculate on two possible explanations for this higher response. The first explanation involves a different spectroscopic response[46,47] from the initially formed PI1 species than from the subsequently formed PI1I2 species, which could be corroborated by the presence of a hydrogen bond connecting the side chain of Thr-309 with the heme-ligating imidazole nitrogen of ketoconazole in the PI1 simulation. Indeed, a computational model based on the LIE0 binding affinities and on the PI1 species having a 40% larger spectroscopic response than the PI1I2 species yields an improved agreement with the experiment (Figure 7). An alternative explanation involves the inactivation of a certain portion of CYP3A4 molecules for direct heme binding, effectively leading to a lower overall protein concentration. Again, a computational LIE0 model in which 20% of CYP3A4 enzymes are inactivated provides a good agreement with the experiment (Figure 7).

In addition, we investigate whether the introduction of the empirical parameter γ was crucial for the success of the LIE0 model. Consequently, the LIE1 model (Table 4) was developed by optimizing the α and β parameters in eqs 1 and 3−6 to obtain the best agreement with the binding free energies of the LIE0 model. By almost doubling the parameter values, the order of binding affinities could be reproduced. Next, we explored the role of preorganized electrostatics in Cytochrome P450 inhibition. CYP3A4 was found to be electrostatically preorganized to bind ketoconazole in the position of inhibitor I regardless of the binding-site occupancy (Table 3). CYP3A4 binding of ketoconazole in the position of inhibitor II is favored by preorganized electrostatics to a much lesser extent—again regardless of the binding-site occupancy. Since polar solvents are not electrostatically preorganized to accommodate solute molecules, preorganized electrostatics seems to be an additional driving force responsible for ketoconazole binding. The LRA1 model (Table 4) including the preorganized electrostatic contribution was developed by optimizing the α and β empirical parameters in eqs 2 and 3−6 to obtain the best agreement with the ketoconazole binding free energies of the LIE0 model. Although the value of the electrostatic parameter β was significantly increased, it still remains considerably lower than the theoretically expected value of 0.5.[21] The order of binding affinities was again successfully reproduced.

Finally, as it is still very likely that the simple two-ligand binding kinetic model provides the correct solution, its predicted binding free energies were applied to optimize the LIE2 model (Table 4). Although the α and β empirical parameters obtained seem unrealistically big, it is reassuring to observe that the order of binding affinities remains unaffected. The simple two-ligand binding kinetic model was also used to optimize the LRA2 model. Please note that the corresponding electrostatic parameter β of 0.43 was obtained, which is identical to the value recommended by Åqvist and co-workers[48] for LIE binding calculations with the Gromos87 force field. The order of binding affinities is again retained and a positive homotropic cooperativity of 9.2 kJ mol^{-1} stemming solely from shape complementarity through nonpolar van der Waals interactions is predicted.

4. CONCLUSIONS

A combination of molecular dynamics simulations and free-energy calculations was applied to address the observed positive

homotropic cooperativity of ketoconazole binding to CYP3A4, which is speculated to arise from a direct interaction between the two bound ketoconazole molecules and/or from selecting and locking a specific preexisting conformation of CYP3A4 with a higher affinity for the other ketoconazole molecule.[1,6,7] Indeed, the presence of a ketoconazole molecule bound to the position of inhibitor II was found to be responsible for maintaining the conformation of CYP3A4 close to its original crystal structure. Moreover, the binding of the first ketoconazole molecule was established to increase the affinity for the binding of the subsequent ketoconazole molecule by 5 kJ mol^{-1} through shape complementarity represented by van der Waals interactions, which explains and quantifies the experimentally observed cooperative behavior of CYP3A4. All in all, the calculated binding free energies were found to be in good agreement with the values predicted from a simple two-ligand binding kinetic model as well as to successfully reproduce the experimental titration curve.[10] This confirms the general applicability of rapid free-energy methods to study challenging biomolecular systems like CYPs that are characterized by a large flexibility and malleability of their active sites.[12,32,49,50]

Shape complementarity through nonpolar van der Waals interactions was identified as the main driving force of ketoconazole binding to CYP3A4, which seems to be in line with the promiscuous nature of this enzyme.[3] Electrostatic interactions disfavor the binding event even though several hydrogen bonds and other polar contacts were detected with various active-site residues and water molecules, inducing a proper orientation of ketoconazole inhibitors in the binding pocket. Moreover, preorganized electrostatics[19,20] of the CYP3A4 active site was recognized as yet another contributing factor to tight ketoconazole binding at least in the position of inhibitor I. It was further observed that the CYP3A4 active site allows for a more favorable intramolecular ketoconazole interaction energy than observed free in solution, which was attributed to the mainly nonpolar interactions and to the malleability of the active site. These results provide a novel mechanistic insight into CYP3A4 inhibition at an atomistic level that is indispensable to rationalize and predict the related adverse drug–drug effects, which constitute a major health risk due to CYP3A4 involvement in the metabolism of more than 50% of clinically used drugs.[4]

■ ASSOCIATED CONTENT

Ⓢ Supporting Information

Building block of the ketoconazole inhibitor, figure of the changes in the CYP3A4 active-site volume and structure, figure of CYP3A4 secondary-structure elements, and figure of central member structures of the six largest ketoconazole clusters. This material is available free of charge via the Internet at http://pubs.acs.org.

■ AUTHOR INFORMATION

Corresponding Author
*E-mail: chris.oostenbrink@boku.ac.at. Telephone: +43-1-476548302. Fax: +43-1-476548309.

Notes
The authors declare no competing financial interest.

■ REFERENCES

(1) de Montellano, P. R. O. *Cytochrome P450: Structure, Function, and Biochemistry*; Kluwer Academic/Plenum Publishers: New York, 2005.

(2) Denisov, I. G.; Makris, T. M.; Sligar, S. G.; Schlichting, I. Structure and Chemistry of Cytochrome P450. *Chem. Rev.* **2005**, *105*, 2253−2277.

(3) Guengerich, F. P. Cytochrome P450 and Chemical Toxicology. *Chem. Res. Toxicol.* **2008**, *21*, 70−83.

(4) Zhou, S.; Chan, S. Y.; Goh, B. C.; Chan, E.; Duan, W.; Huang, M.; McLeod, H. L. Mechanism-Based Inhibition of Cytochrome P450 3A4 by Therapeutic Drugs. *Clin. Pharmacokinet.* **2005**, *44*, 279−304.

(5) Groopman, J. D.; Kensler, T. W.; Wild, C. P. Protective Interventions to Prevent Aflatoxin-Induced Carcinogenesis in Developing Countries. *Ann. Rev. Public Health* **2008**, *29*, 187−203.

(6) Atkins, W. M.; Wang, R. W.; Lu, A. Y. H. Allosteric Behavior in Cytochrome P450-Dependent in Vitro Drug−Drug Interactions: A Prospective Based on Conformational Dynamics. *Chem. Res. Toxicol.* **2001**, *14*, 338−347.

(7) Atkins, W. M.; Lu, W. D.; Cook, D. L. Is There a Toxicological Advantage for Non-hyperbolic Kinetics in Cytochrome P450 Catalysis? Functional Allostery from "Distributive Catalysis". *J. Biol. Chem.* **2002**, *277*, 33258−33266.

(8) Silgar, S. G. Coupling of Spin, Substrate, and Redox Equilibriums in Cytochrome P450. *Biochemistry* **1976**, *15*, 5399−5406.

(9) Sevrioukova, I. F.; Poulos, T. L. Structure and Mechanism of the Complex between Cytochrome P4503A4 and Ritonavir. *Proc. Natl. Acad. Sci. U.S.A.* **2010**, *107*, 18422−18427.

(10) Isin, E. M.; Guengerich, F. P. Multiple Sequential Steps Involved in the Binding of Inhibitors to Cytochrome P450 3A4. *J. Biol. Chem.* **2007**, *282*, 6863−6874.

(11) Ekroos, M.; Sjoegren, T. Structural Basis for Ligand Promiscuity in Cytochrome P450 3A4. *Proc. Natl. Acad. Sci. U.S.A.* **2006**, *103*, 13682−13687.

(12) Stjernschantz, E.; Vermeulen, N. P. E.; Oostenbrink, C. Computational Prediction of Drug Binding and Rationalisation of Selectivity towards Cytochromes P450. *Expert Opin. Drug Metab. Toxicol.* **2008**, *4*, 513−527.

(13) Åqvist, J.; Medina, C.; Samuelsson, J.-E. A New Method for Predicting Binding Affinity in Computer-Aided Drug Design. *Protein Eng.* **1994**, *7*, 385−391.

(14) Carlson, H. A.; Jorgensen, W. L. An Extended Linear Response Method for Determining Free Energies of Hydration. *J. Phys. Chem.* **1995**, *99*, 10667−10673.

(15) Bren, M.; Florian, J.; Mavri, J.; Bren, U. Do all pieces make a whole? Thiele cumulants and the free energy decomposition. *Theor. Chem. Acc.* **2007**, *117*, 535−540.

(16) Bren, U.; Martinek, V.; Florian, J. Decomposition of the Solvation Free Energies of Deoxyribonucleoside Triphosphates Using the Free Energy Perturbation Method. *J. Phys. Chem. B* **2006**, *110*, 12782−12788.

(17) Lee, F. S.; Chu, Z.-T.; Bolger, M. B.; Warshel, A. Calculations of Antibody-Antigen Interactions: Microscopic and Semi-Microscopic Evaluation of the Free Energies of Binding of Phosphorylcholine Analogs to McPC603. *Protein Eng.* **1992**, *5*, 215−228.

(18) Bren, U.; Lah, J.; Bren, M.; Martinek, V.; Florian, J. DNA Duplex Stability: The Role of Preorganized Electrostatics. *J. Phys. Chem. B* **2010**, *114*, 2876–2885.

(19) Warshel, A.; Florian, J. Computer Simulations of Enzyme Catalysis: Finding out what has been Optimized by Evolution. *Proc. Natl. Acad. Sci. U.S.A.* **1998**, *95*, 5950–5955.

(20) Warshel, A. *Computer Modelling of Chemical Reactions in Enzymes and Solutions*; John Wiley & Sons: New York, 2001.

(21) Leach, A. R. *Molecular Modelling: Principles and Applications*; Pearson: Harlow, 2001.

(22) Schmid, N.; Christ, C. D.; Christen, M.; Eichenberger, A. P.; van Gunsteren, W. F. Architecture, Implementation and Parallelisation of the GROMOS Software for Biomolecular Simulation. *Comput. Phys. Commun.* **2012**, *183*, 890–903.

(23) Berendsen, H. J. C.; Postma, J. P. M.; van Gunsteren, W. F.; Hermans, J. *Intermolecular Forces*; Reidel: Dordrecht, The Netherlands, 1981.

(24) Amadei, A.; Chillemi, G.; Ceruso, M. A.; Grottesi, A.; Di Nola, A. Molecular Dynamics Simulations with Constrained Roto-Translational Motions: Theoretical Basis and Statistical Mechanical Consistency. *J. Chem. Phys.* **2000**, *112*, 9.

(25) Berendsen, H. J. C.; Postma, J. P. M.; van Gunsteren, W. F.; DiNola, A.; Haak, J. R. Molecular Dynamics with Coupling to an External Bath. *J. Chem. Phys.* **1984**, *81*, 3684–3590.

(26) Ryckaert, J. P.; Ciccotti, G.; Berendsen, H. J. C. Numerical Integration of the Cartesian Equations of Motion of a System with Constraints: Molecular Dynamics of n-Alkanes. *J. Comput. Phys.* **1977**, *23*, 327–341.

(27) Tironi, I. G.; Sperb, R.; Smith, P. E.; van Gunsteren, W. F. A Generalized Reaction Field Method for Molecular Dynamics Simulations. *J. Chem. Phys.* **1995**, *102*, 5451–5459.

(28) Heinz, T. N.; van Gunsteren, W. F.; Huenenberger, P. H. Comparison of Four Methods to Compute the Dielectric Permittivity of Liquids from Molecular Dynamics Simulations. *J. Chem. Phys.* **2001**, *115*, 1125.

(29) Yano, J. K.; Wester, M. R.; Schoch, G. A.; Griffin, K. J.; Stout, C. D.; Johnson, E. F. The Structure of Human Microsomal Cytochrome P450 3A4 Determined by X-ray Crystallography to 2.05-Å Resolution. *J. Biol. Chem.* **2004**, *279*, 38091–38094.

(30) Williams, P. A.; Cosme, J.; Vinkovic, D. M.; Ward, A.; Angove, H. C.; Day, P. J.; Vonrhein, C.; Tickle, I. J.; Jhoti, H. Crystal Structures of Human Cytochrome P450 3A4 Bound to Metyrapone and Progesterone. *Science* **2004**, *305*, 683–686.

(31) Dundas, J.; Ouyang, Z.; Tseng, J.; Binkowski, A.; Turpaz, Y.; Liang, J. CASTp: computed atlas of surface topography of proteins with structural and topographical mapping of functionally annotated residues. *Nucleic Acids Res.* **2006**, *34*, W116–W118.

(32) Hendrychova, T.; Berka, K.; Navratilova, V.; Anzenbacher, P.; Otyepka, M. Dynamics and Hydration of the Active Sites of Mammalian Cytochromes P450 Probed by Molecular Dynamics Simulations. *Curr. Drug Metab.* **2012**, *13*, 177–189.

(33) Wade, R. C.; Winn, P. J.; Schlichting, I.; Sudarako, A. A Survey of Active Site Access Channels in Cytochromes P450. *J. Inorg. Biochem.* **2004**, *98*, 1175–1182.

(34) Schlitter, J. Estimation of Absolute and Relative Entropies of Macromolecules Using the Covariance Matrix. *Chem. Phys. Lett.* **1993**, *215*, 617–621.

(35) Baron, R.; van Gunsteren, W. F.; Huenenberger, P. H. Estimating the Configurational Entropy from Molecular Dynamics Simulations: Anharmonicity and Correlation Corrections to the Quasi-Harmonic Approximation. *Trends. Phys. Chem.* **2006**, *11*, 87–122.

(36) Park, H.; Lee, S.; Suh, J. Structural and Dynamical Basis of Broad Substrate Specificity, Catalytic Mechanism, and Inhibition of Cytochrome P450 3A4. *J. Am. Chem. Soc.* **2005**, *127*, 13634–13642.

(37) Fishelovitch, D.; Hazan, C.; Shaik, S.; Wolfson, H. J.; Nussinov, R. Structural Dynamics of the Cooperative Binding of Organic Molecules in the Human Cytochrome P450 3A4. *J. Am. Chem. Soc.* **2007**, *129*, 1602–1611.

(38) Brooks, B. R.; Janežič, D.; Karplus, M. Harmonic Analysis of Large Systems. I. Methodology. *J. Comput. Chem.* **1995**, *16*, 1522–1542.

(39) Janežič, D.; Brooks, B. R. Harmonic Analysis of Large Systems. II. Comparison of Different Protein Models. *J. Comput. Chem.* **1995**, *16*, 1543–1553.

(40) Janežič, D.; Venable, R. M.; Brooks, B. R. Harmonic Analysis of Large Systems. III. Comparison with Molecular Dynamics. *J. Comput. Chem.* **1995**, *16*, 1554–1566.

(41) Peter, C.; Oostenbrink, C.; van Dorp, A.; van Gunsteren, W. F. Estimating Entropies from Molecular Dynamics Simulations. *J. Chem. Phys.* **2004**, *120*, 2652–2661.

(42) Daura, X.; van Gunsteren, W. F.; Mark, A. E. Folding–Unfolding Thermodynamics of a β-Heptapeptide from Equilibrium Simulations. *Proteins* **1999**, *34*, 269–280.

(43) Csermely, P.; Palotai, R.; Nussinov, R. Induced Fit, Conformational Selection and Independent Dynamic Segments: An Extended View of Binding Events. *Trends Biochem. Sci.* **2010**, *35*, 539–546.

(44) Vasanthanathan, P.; Olsen, L.; Jorgensen, F. S.; Vermeulen, N. P. E.; Oostenbrink, C. Computational Prediction of Binding Affinity for CYP1A2-Ligand Complexes Using Empirical Free Energy Calculations. *Drug Metab. Dispos.* **2010**, *38*, 1347–1354.

(45) Cornish-Bowden, A. *Fundamentals of Enzyme Kinetics*; Portland Press: London, 2004.

(46) Locuson, C. W.; Hutzler, J. M.; Tracy, T. S. Visible Spectra of Type II Cytochrome P450-Drug Complexes: Evidence that "Incomplete" Heme Coordination Is Common. *Drug Metab. Dispos.* **2007**, *35*, 614–622.

(47) Leach, A. G.; Kidley, N. J. Quantitatively Interpreted Enhanced Inhibition of Cytochrome P450s by Heteroaromatic Rings Containing Nitrogen. *J. Chem. Inf. Model.* **2011**, *51*, 1048–1063.

(48) Hansson, T.; Marelius, J.; Åqvist, J. Ligand Binding Affinity Prediction by Linear Interaction Energy Methods. *J. Comput.-Aided Mol. Des.* **1998**, *12*, 27–35.

(49) Oostenbrink, C.; de Ruiter, A.; Hritz, J.; Vermeulen, N. Malleability and Versatility of Cytochrome P450 Active Sites Studied by Molecular Simulations. *Curr. Drug Metab.* **2012**, *13*, 190–196.

(50) Guengerich, F. P. A Malleable Catalyst Dominates the Metabolism of Drugs. *Proc. Natl. Acad. Sci. U.S.A.* **2006**, *103*, 13565–13566.

(51) Allen, M. P.; Tildesley, D. J. *Computer Simulation of Liquids*; Clarendon Press: Oxford, 1987.